Electronic supplementary information (ESI)

Hole-transporting alternating copolymers for perovskite solar cells: thia[5]helicene comonomer outperforms planar perylothiophene analog

Lifei He, Yuyan Zhang,* Bing Zhang, Tianyu Li, Yaohang Cai, Ming Ren, Jing Zhang, Peng Wang* and Yi Yuan*

State Key Laboratory of Silicon and Advanced Semiconductor Materials, Department of Chemistry, Zhejiang University, Hangzhou 310058, China.

_____

* Corresponding authors.

E-mail addresses: yuyanzhang@zju.edu.cn, pw2015@zju.edu.cn, yyuan@zju.edu.cn.

1 Experimental section

1.1 Reagents and materials

Tris(dibenzylideneacetone)dipalladium (Pd$_2$(dba)$_3$, 98%, Energy Chemical), tris(3-methoxyphenyl)phosphine (P(o-MeOPh)$_3$, 98%, Energy Chemical), N,N,N',N'-tetramethylethylenediamine (TMEDA, 99%, Energy Chemical), pivalic acid (PivOH, 99%, Energy Chemical), cesium carbonate (Cs$_2$CO$_3$, 99.9%, Energy Chemical), disodium dihydrogen ethylenediaminetetraacetate dihydrate (EDTA, 99%, Energy Chemical), deuterated tetrahydrofuran (THF-d_8, 99.8%, Energy Chemical), tetrahydrofuran (THF, 99%, Sinopharm Chemical Reagent Co., Ltd), acetone ($\geq$ 99.5%, Sinopharm Chemical Reagent Co., Ltd), ethanol (99.7%, Aladdin), chlorobenzene (99.8%, Acros Organics), 4-tert-butylpyridine (TBP, 96%, Sigma-Aldrich), benzocyclobutene (BCB, 98%, Energy Chemical), tin oxide (SnO$_2$, 15% in H$_2$O colloidal dispersion, Alfa Aesar), lead iodide (PbI$_2$, 99.99%, TCI), rubidium chloride (RbCl, 99.9%, 3A), formamidinium iodide (FAI, 99.0%, Greatcell Solar), methylammonium chloride (MACl, $\geq$ 99.5%, Xi'an Polymer Light Technology Corp.), N,N-dimethylformamide (DMF, 99.8%, Aldrich), dimethyl sulfoxide (DMSO, 99.9%, Aldrich), phenethylammonium iodide (PEAI, 98%, TCI), isopropyl alcohol (IPA, > 99.8%, Sigma-Aldrich), PEDOT:PSS (AI 4083, Heraeus® Clevios), $N^2,N^2,N^{2'},N^{2'},N^7,N^7,N^{7'},N^{7'}$-octakis(4-methoxyphenyl)-9,9'-spirobi[fluorene]-2,2',7,7'-tetraamine (spiro-OMeTAD, 99.8%, Xi'an Polymer Light Technology Corp.), poly[bis(4-phenyl)(2,4,6-trimethylphenyl)amine] (PTAA, $M_n \sim$ 10 kDa, Merck), polystyrene (PS, typical $M_w \sim$ 280 kDa, Sigma-Aldrich), and other solvents were procured from commercial sources and employed without additional purification. Deionized water with a resistivity greater than 18 MΩ cm was supplied by a UPR-II-10T Ultrapure water system (ULUPURE). The compounds 5,9-dibromodinaphtho[2,1-b:1',2'-d]thiophene (2Br-T5H),[1] 3,10-dibromoperylo[1,12-b,c,d]thiophene (2Br-PET),[1] 3,7-bis(2,3-dihydrothieno[3,4-b][1,4]dioxin-5-yl)-10-(2-octyldodecyl)-10H-phenoxazine (E-POZ-E),[2] and 4-tert-butylpyridinium bis(trifluoromethanesulfonyl)imide (TBPHTFSI)[3] were synthesized following established protocols from the literature.

1.2 General instrumentation

The ^{1}H and ^{13}C nuclear magnetic resonance (NMR) spectra were obtained using an AVANCE III 400 NMR spectrometer (Bruker). Attenuated total reflection-Fourier transform infrared (ATR-FTIR) spectra were recorded on either a Vector 22 FTIR spectrometer (Bruker) or a Nicolet™ iS50 FTIR spectrometer (Thermo Fisher). The weight percentages of carbon, hydrogen, and nitrogen were determined using the Vario Micro cube element analyzer (Elementar Analysensysteme GmbH). Ultraviolet-visible (UV-vis) absorption spectra were acquired with a Cary 8454 spectrophotometer (Agilent). High-temperature gel permeation chromatography (HT-GPC)

measurements were performed using the PL-GPC220 instrument (Polymer Laboratories Ltd.) with 1,2,4-trichlorobenzene as the solvent. Differential scanning calorimetry measurements were conducted on a DSC Q100 V9.7 Build 291 instrument (TA Instruments) under a flowing nitrogen atmosphere, employing a heating rate of $10°C\ min^{-1}$. Time-resolved photoluminescence traces were recorded using the Life-Spec-II fluorescence spectrometer (Edinburgh Instruments). Scanning electron microscope images were obtained with a SU-70 field emission scanning electron microscope (Hitachi). X-ray diffraction patterns of thin films were measured using a SmartLab diffractometer (Rigaku), employing Cu Kα radiation (λ = 0.15418 nm) at 7200 W power (40 kV, 180 mA). The thicknesses of thin films were measured using a D-500 stylus profilometer (KLA-Tencor). The water contact angles of thin films were determined using a DropMeter™ A-100P contact angle meter (Maist Co. Ltd.). Polarizing optical microscope images were captured on an SDPTOP CX40P system (Sunny Optical), while fluorescence optical microscope images were recorded using an ECLIPSE Ti-U system (Nikon).

1.3 Synthesis

1.3.1 p-T5H-E-POZ-E

A Schlenk reaction vessel was charged with 2Br-T5H (884.0 mg, 2.00 mmol), E-POZ-E (1.5 g, 2.00 mmol), $Pd_2(dba)_3$ (91.6 mg, 0.10 mmol), P(o-MeOPh)$_3$ (140.9 mg, 0.40 mmol), TMEDA (116.0 mg, 1.00 mmol), PivOH (1.0 g, 10.00 mmol), Cs_2CO_3 (3.3 g, 10.00 mmol), and toluene (80 mL). The reaction vessel underwent three cycles of evacuation and argon purging. Subsequently, the reaction mixture was stirred for 6 hours at 110°C. After cooling to room temperature, the solution was concentrated under vacuum and sequentially washed with a 0.1 M EDTA aqueous solution, water, and methanol. The resulting residue underwent purification through a silica gel column, utilizing elution with toluene/petroleum ether 60–90°C (v/v, 1/1) and toluene. The toluene fraction was collected, concentrated to a reduced volume, and added dropwise into vigorously stirred methanol (200 mL). The resulting mixture underwent filtration, followed by drying, yielding the desired product as an orange solid (1.7 g, 82%). Melting point: > 300°C. ^{1}H NMR (400 MHz, THF-d_8) δ: 8.51−8.34 (m, 2H), 7.97−7.75 (m, 2H), 7.69−7.56 (m, 2H), 7.34−7.22 (m, 4H), 7.12−6.93 (m, 4H), 6.68−6.22 (m, 2H), 4.32 (s, 4H), 4.18 (s, 4H), 3.46 (s, 2H), 1.89 (br, 1H), 1.38−1.04 (m, 32H), and 0.72−0.68 (m, 6H) ppm. ^{13}C NMR (100 MHz, THF-d_8) δ: 145.87, 140.66, 139.31, 138.91, 133.28, 132.02, 131.80, 131.76, 131.39, 131.18, 130.87, 128.74, 127.38, 127.03, 126.35, 125.88, 123.97, 121.85, 117.74, 113.92, 113.34, 112.94, 112.87, 111.87, 65.95, 65.65, 48.63, 36.48, 33.07, 32.76, 31.22, 30.81, 30.74, 30.70, 30.51, 30.50, 27.79, 23.77, and 14.67 ppm. ATR-FTIR (film) ν_{max}: 2921, 2851, 1490, 1432, 1360, 1280, 1089, 869, 800, and 755 cm^{-1}. UV-vis (chlorobenzene) λ_{max}: 367 and 459 nm. Elemental analysis calcd. for $(C_{64}H_{65}NO_5S_3)_n$: C 75.04, H 6.40, N 1.37. Found: C 75.05, H 6.45, N 1.40.

1.3.2 p-PET-E-POZ-E

A Schlenk reaction vessel was charged with 2Br-PET (880.0 mg, 2.00 mmol), E-POZ-E (1.5 g, 2.00 mmol), $Pd_2(dba)_3$ (91.6 mg, 0.10 mmol), P(o-MeOPh)$_3$ (140.9 mg, 0.40 mmol), TMEDA (116.0 mg, 1.00 mmol), PivOH (1.0 g, 10.00 mmol), Cs_2CO_3 (3.3 g, 10.00 mmol), and toluene (80 mL). The reaction vessel underwent three cycles of evacuation and argon purging. Subsequently, the reaction mixture was stirred for 6 hours at 110°C. After cooling to room temperature, the solution was concentrated under vacuum and sequentially washed with a 0.1 M EDTA aqueous solution, water, and methanol. The resulting residue underwent purification through a silica gel column, employing elution with toluene and toluene/THF (v/v, 1/1). The toluene/THF fraction was collected, concentrated to a reduced volume, and introduced dropwise into vigorously stirred methanol (200 mL). The resulting mixture underwent filtration, followed by drying, yielding the desired product as a red solid (899.0 mg, 44%). Melting point: > 300°C. ^{1}H NMR (400 MHz, THF-d_8) δ: 8.56–8.45 (m, 2H), 8.31–8.20 (m, 2H), 8.16–8.07 (m, 2H), 7.75–7.63 (m, 2H), 7.16–6.98 (m, 4H), 6.53–6.42 (m, 2H), 4.34–4.16 (m, 8H), 3.42–3.33 (m, 2H), 1.91–1.86 (br, 1H), 1.34–1.10 (m, 32H), and 0.79–0.74 (m, 6H) ppm. ^{13}C NMR (100 MHz, THF-d_8) δ: 144.29, 142.19, 138.98, 137.40, 133.45, 131.72, 131.69, 131.64, 131.49, 130.22, 130.15, 129.33, 129.06, 128.36, 126.18, 125.83, 123.55, 120.54, 115.97, 115.91, 112.37, 111.69, 111.62, 111.31, 64.40, 64.36, 47.03, 34.92, 31.53, 31.24, 29.68, 29.66, 29.27, 29.18, 28.96, 26.28, 26.26, 22.21, and 13.12 ppm. ATR-FTIR (film) v_{max}: 2923, 2851, 1488, 1429, 1358, 1278, 1065, 869, 800, and 757 cm^{-1}. UV-vis (chlorobenzene) λ_{max}: 478 nm. Elemental analysis calcd. for $(C_{64}H_{63}NO_5S_3)_n$: C 75.19, H 6.21, N 1.37. Found: C 75.30, H 6.24, N 1.39.

1.4 Ultraviolet photoelectron spectroscopy (UPS) measurements

The indium-doped tin oxide (ITO) glass was cleaned through sequential sonication in deionized water, acetone, and ethanol, each for a duration of 10 minutes. Following the thorough cleaning process, the substrates underwent exposure to UV-ozone for 15 minutes before utilization. A layer of PEDOT:PSS was spin-coated onto the ITO substrate and annealed at 150°C for 15 minutes. Subsequent to cooling to room temperature, a semiconducting polymer layer was deposited through spin coating a chlorobenzene solution. This solution, composed of either 40 mg mL^{-1} of p-T5H-E-POZ-E or p-PET-E-POZ-E dissolved in chlorobenzene, facilitated the polymer layer deposition. The UPS spectra were acquired utilizing an ESCALAB XI+ instrument from Thermo Fisher.

1.5 Hole density measurements

The determination of hole density (p) in the pristine polymeric semiconductor involves impedance spectra analysis of a metal-insulator-semiconductor (MIS) device. The MIS device is structured as n^{++}-Si/SiO$_2$/p-BCB/HTM/Au. The p-BCB layer is applied atop SiO$_2$ through spin-coating a chlorobenzene solution (1 mg mL^{-1}) at 4000 rpm

for 30 s, followed by annealing at 250°C for 1 h. The polymeric semiconductor solution comprises 40 mg mL^{-1} of either p-T5H-E-POZ-E or p-PET-E-POZ-E, combined with 132 mM of TBP. Subsequently, the solution is spin-coated onto the p-BCB layer at 3000 rpm for 30 s, and gold contacts (~120 nm) are thermally evaporated. Impedance spectra are recorded using an Autolab PGSTAT302N electrochemical workstation, covering a frequency range from 10 Hz to 3 MHz with a small perturbation of 20 mV. The corrected capacitance (C) is determined using the equation: $C = -\dfrac{1}{\omega}[\dfrac{Z''-\omega L_i}{(Z'-R_s)^2+(Z''-\omega L_i)^2}]$, where ω represents the angular frequency, Z' and Z'' denote the real and imaginary impedance components, R_s is the series resistance, and L_i is the parasitic inductance. The p value is quantified through the Mott-Schottky plot, expressed as $p = \dfrac{2}{q\varepsilon_r\varepsilon_0 \dfrac{d(A/C)^2}{dV}}$. Here, q is the elementary charge, ε_r is the relative permittivity, ε_0 is the vacuum permittivity, and A corresponds to the area of MIS device.

Determining the p value for a polymeric semiconductor composite film containing TBPHTFSI using the MIS device posed a significant challenge. To overcome this, we employed a comparative approach focusing on the quadratic integral intensities of electron paramagnetic resonance (EPR) signals from polymeric semiconductor films, both with and without TBPHTFSI. The benchmark for estimation was the established p value for a pristine polymeric semiconductor film. For EPR spectrum measurement, a chlorobenzene solution was drop-cast onto a 2 cm × 2 cm microslide. Subsequently, the polymeric semiconductor-coated microslide was crushed and transferred into a borosilicate glass tube. The chlorobenzene solution comprised TBP (132 mM) and a semiconducting polymer with a concentration set at 40 mg mL^{-1}. The weight ratios of TBPHTFSI to polymeric semiconductor were systematically adjusted to 0:100, 5:95, 10:90, or 15:85. EPR measurements were conducted using a Bruker A300-10/12 spectrometer.

1.6 Direct-current electrical conductivity measurements

To assess direct-current electrical conductivity (σ), interdigital gold electrodes underwent a coating process involving the application of a polymeric semiconductor layer. The polymeric semiconductor layer was achieved through spin-coating a chlorobenzene solution at a speed of 3000 rpm. The interdigital gold electrode, consisting of 119 channels, featured a channel length (L) of 1.5 mm, a channel width (W) of 10 μm, and a channel thickness (t) of 110 nm. The chlorobenzene solution comprised TBP (132 mM) and a semiconducting polymer with a concentration set at 40 mg mL^{-1}. The weight ratios of TBPHTFSI to polymeric semiconductor were systematically adjusted to 0:100, 5:95, 10:90, or 15:85. Before measurements, the devices were stored in a dry air environment

(< 5% relative humidity) for seven days. Current–voltage (*I–V*) curves were acquired at various temperatures by applying a potential bias ranging from −1.0 V to 1.0 V. The σ value was determined by calculating the slope (*s*) obtained from linear fitting of the *I–V* curve, using the equation $\sigma = sW/nLt$.

1.7 Fabrication of solar cells

The cleaned ITO substrates were subjected to a 15-minute UV-ozone treatment prior to utilization. The SnO_2 colloid dispersion was diluted with deionized water in a volumetric ratio of 1:4. The dispersion underwent filtration through a 0.2 μm polytetrafluoroethylene filter. Subsequently, the solution was spin-coated onto the ITO substrate at 4000 rpm for a duration of 30 seconds, followed by an annealing process at 150°C for 30 minutes in ambient air. After the UV-ozone treatment, the glass/ITO/SnO_2 substrate transitioned into a glove box, where a controlled dry air environment with approximately 3% humidity was maintained. The $FAPbI_3$ perovskite layer was constructed through a two-step spin-coating process. Initially, a solution containing 1.5 M PbI_2 and 7.5 mM RbCl in a mixed solvent of DMF and DMSO (*v/v*, 9/1) was spin-coated onto the SnO_2 substrate at 1500 rpm for 30 seconds, followed by annealing at 70°C for 1 minute. Upon reaching room temperature, an IPA solution containing FAI (90 mg mL^{-1}) and MACl (13.5 mg mL^{-1}) was spin-coated onto the PbI_2 layer at 1800 rpm for 30 seconds. The resulting film underwent annealing at 150°C for 30 minutes, culminating in the formation of the light absorption layer based on $FAPbI_3$, featuring a minor quantity of $(PbI_2)_2RbCl$.[4] For the passivation layer, a solution of PEAI (10 mM) in IPA was spin-coated onto the perovskite surface at a speed of 5000 rpm for 30 seconds.[5] Subsequently, a chlorobenzene solution was spin-coated at 3000 rpm for 30 seconds to deposit a hole transport layer. The chlorobenzene solution was formulated with 40 mg mL^{-1} of p-T5H-E-POZ-E, p-PET-E-POZ-E, PTAA, or 60 mg mL^{-1} of spiro-OMeTAD, in combination with TBP (132 mM) and TBPHTFSI which maintains a weight ratio of 15:85 to organic semiconductor. The gold electrode (~120 nm) was deposited using a shadow mask in a vacuum of $\leq 1 \times 10^{-4}$ Pa. The resultant device, featuring an active area of 0.26 cm^2, underwent lamination with a high-quality anti-reflective film on the glass side. The gold side was then carefully covered with waterproof adhesive tape and sealed with epoxy adhesive (3M).

1.8 Photocurrent–voltage characteristic and external quantum efficiency

The photocurrent density–voltage (*J–V*) characteristics were assessed using a Keithley 2400 source meter, with measurements automated through Labview 14.0. To mimic AM1.5G sunlight conditions, a LS1000-4S-AM solar simulator from Solar Light Company was employed. The photoactive area was defined by a black metal mask with an aperture area of 0.16 cm². Both reverse scan (1.2V→0V, step 0.005V) and forward scan (0V→1.2V, step 0.005V) were conducted on the cells. External quantum efficiency (EQE) measurements were performed using

an Omni-λ300 monochromator (Zolix) in conjunction with a 150 W xenon lamp (Zolix) for monochromatic light supply. The photocurrent was recorded using a Keithley 2400 source meter. For intensity measurements of the monochromatic light, a Hamamatsu S1337-1010BQ silicon diode, calibrated at the National Institute of Metrology, was utilized.

1.9 Thermal stability, operational stability, and humidity stability

For the assessment of thermal stability, the perovskite solar cells were stored within an FD56 oven (Binder) set at 85°C. The ambient humidity levels varied between 40% and 90%. Intermittent $J–V$ measurements were performed under AM1.5G conditions at room temperature. For maximum power point tracking (MPPT), a 16-channel photovoltaic tracking system (YH Electronic Equipment Business) was employed in tandem with an SLS-LED-80A solar simulator (Solar Scientific Instrument High-tech Co., Ltd.). This experimental configuration was integrated with a nitrogen-filled glovebox to ensure controlled environmental conditions. MPPT data were acquired at 30-minute intervals utilizing the perturb and observe method. To assess the humidity stability at ambient temperature, encapsulated PSCs were positioned within a sealed buckle box filled with water at the bottom, ensuring an internal humidity approximating 100%. Concurrently, an analogous arrangement was subjected to an 85°C test to scrutinize the humidity endurance of PSCs under elevated temperature, maintaining internal humidity at near saturation. Periodic assessments of the cell performance were conducted through the acquisition of $J–V$ curves under simulated AM1.5G sunlight at ambient temperature.

1.10 Solar cell disassembly

The disassembly procedure for encapsulated solar cells entailed the sequential removal of epoxy adhesive and waterproof adhesive tape, unintentionally leading to partial gold electrode removal. Subsequently, a layer of magic tape (Scotch, 3M) was applied onto the residual gold layer. Peeling off the magic tape resulted in the complete elimination of the gold layer.

1.11 Nanoindentation measurements

The Young′s moduli of polymer composites incorporating 15 wt% TBPHTFSI were determined utilizing the nanoindentation method. Experiments were conducted at room temperature using an iNano nanoindenter (KLA), featuring a diamond Berkovich tip with an approximate tip radius of 20 nm. Prior to each test, the indenter's tip was calibrated against fused silica to maintain thermal drift below 0.05 nm s^{-1}. The load function comprised a 10-second loading phase followed by a 10-second unloading phase. Throughout testing, both the applied force and depth of indentation into the samples were continuously recorded. Young′s modulus was determined by fitting the unloading curve of each sample, employing the well-established Oliver–Pharr method.[6]

2 Theoretical calculations

2.1 Density functional theory calculations

The molecule geometries were optimized using the Gaussian 16 program suite within the framework of periodic boundary condition-density functional theory at the B3LYP/6-311G(d,p) level. The frontier molecular orbitals were visualized via GaussView 5.0.

2.2 Molecular dynamics and Monte Carlo simulations

The construction of polymer chains, each with a molecular weight of approximately 10 kDa or 5 kDa, was accomplished using the Build Polymer tool within Material Studio 8.0. Subsequently, the Amorphous Cell module was employed to generate a cubic box with periodic boundaries. This designated box accommodated either 10 (or 20) polymer chains individually or an assembly of 10 (or 20) polymer chains intricately intertwined with TBPHTFSI molecules, maintaining a weight ratio of 85:15. Molecular dynamics (MD) simulations were conducted using the COMPASS II force field. The investigation of glass transition temperature and diffusion coefficient was further pursued through the FORCITE module in Materials Studio 8.0. The simulation protocol commenced with an NVT simulation at 700 K using a Nose thermostat, followed by an NPT simulation at 700 K employing both a Nose thermostat and a Berendsen barostat. Subsequently, a systematic cooling protocol spanning the temperature range from 700 K to 200 K was implemented, with NVT and NPT simulations conducted at each temperature. Thermodynamic equilibrium was confirmed by recording specific volumes at every stage. The theoretical glass transition temperature was determined through intersection point analysis involving linear fitting lines in the low- and high-temperature regions. Additionally, H_2O or FAI was introduced into the polymer-TBPHTFSI composites, and NVT and NPT simulations were systematically executed. Insights into theoretical diffusion coefficients were derived from the analysis of mean square displacements recorded during the simulations. The Sorption module in Materials Studio 8.0 was utilized for grand canonical Monte Carlo simulations, focusing on the adsorption isotherm to elucidate H_2O solubility. Subsequently, water permeability was determined. Furthermore, simulations involving Young's modulus and cohesive energy density were conducted using the FORCITE module.

3. Supplementary figures and tables
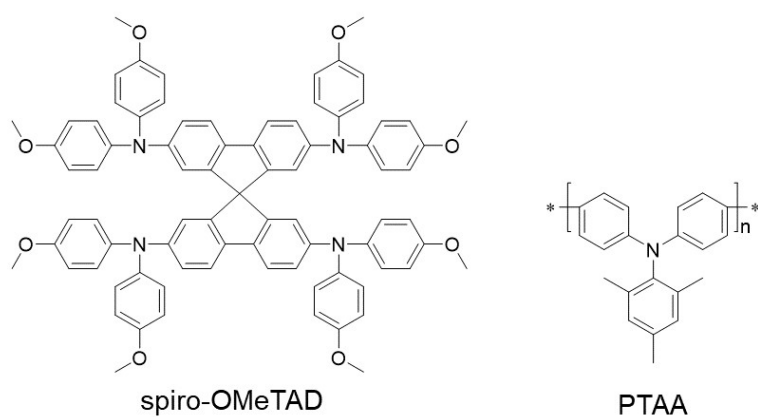
Fig. S1 Chemical structures of the predominantly utilized hole transport materials in n-i-p type perovskite solar cells: molecular semiconductor spiro-OMeTAD and polymeric semiconductor PTAA.
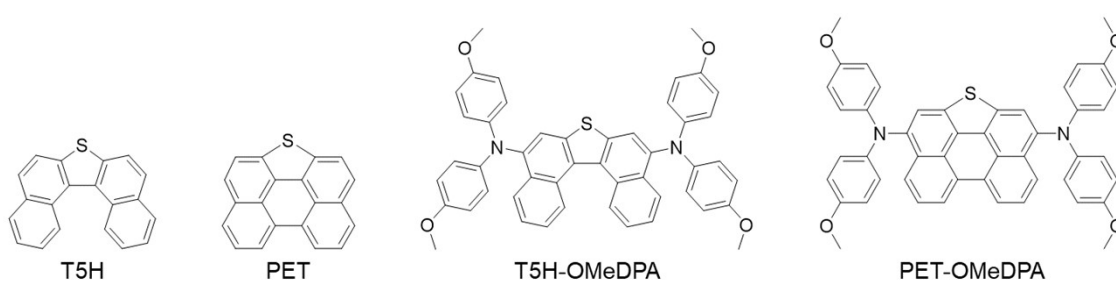
Fig. S2 Chemical structures of molecular semiconductors T5H, PET, T5H-OMeDPA, and PET-OMeDPA.
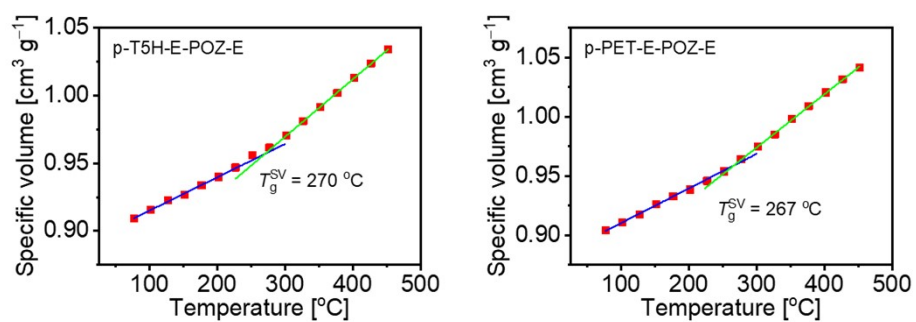
Fig. S3 Temperature-dependent specific volume profiles with linear fits. Blue lines delineate fits in the low-temperature domain, while green lines represent fits in the high-temperature region. The points of intersection between these linear fits unveil the theoretical glass transition temperatures (T_g^{SV})
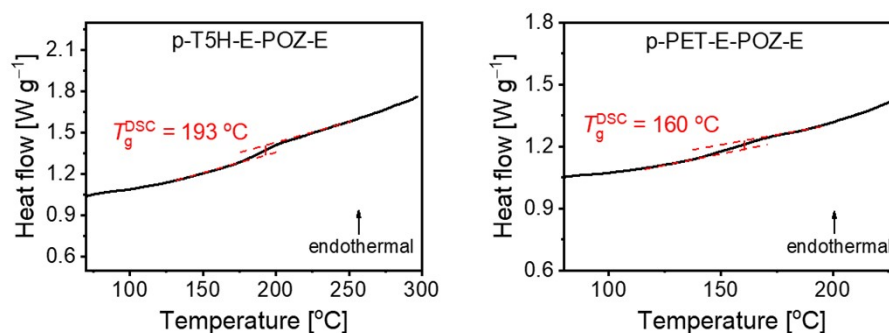
Fig. S4 Differential scanning calorimetry thermograms during the second heatings, with inclusion of glass transition temperatures (T_g^{DSC}).
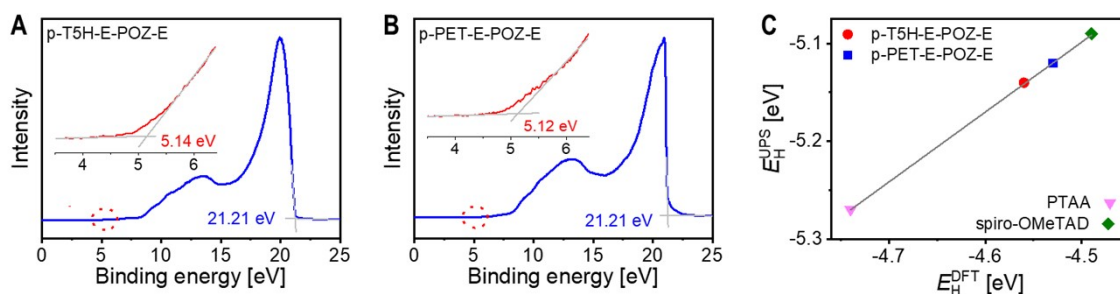
Fig. S5 (A,B) Ultraviolet photoelectron spectra of semiconducting polymer thin films spin-coated onto the ITO/PEDOT:PSS substrate. The spectra have been calibrated, aligning their cutoff edges with the energy of He I photons (21.21 eV). The inset provides an enlarged view of the onset region. The determination of the HOMO energy level (E_H^{UPS}) is grounded on the intersection point between the tangent to the spectrum in the low binding energy range and the baseline parallel to the x-axis. (C) Relationship between the experimentally measured and theoretically calculated HOMO energy levels. E_H^{DFT} denotes the values derived from theoretical calculations utilizing the periodic boundary condition-density functional theory method.
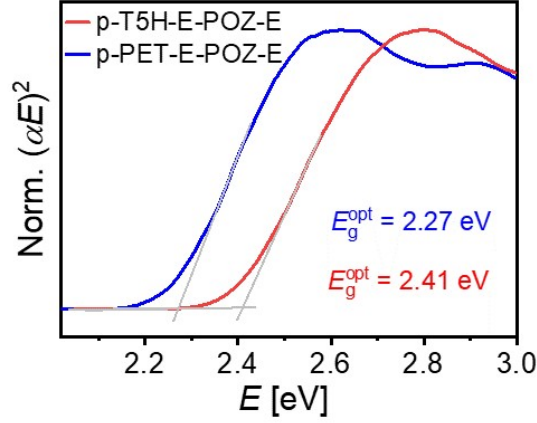
Fig. S6 Tauc plots of semiconducting polymer thin films on quartz substrate. Here, E, α, and E_g^{opt} denote the photon energy, optical absorption coefficient, and optical bandgap, respectively. The determination of E_g^{opt} relies on identifying the intersection point between the tangent drawn to the spectral curve within the lower energy regime and the baseline, which runs parallel to the x-axis.

Table S1. Fitting parameters for photoluminescence decays in glass-supported FAPbI$_3$ films with diverse organic coating layers, along with amplitude-weighted average photoluminescence lifetimes, hole extraction time constants, and hole extraction yields[a]

Sample	τ_1 [ns]	A_1	τ_2 [ns]	A_2	τ [ns]	k_{he} [μs^{-1}]	ϕ_{he} [%]
glass/FAPbI$_3$/PS	2583.1	0.44	5730.0	0.56	4345.4	/	/
glass/FAPbI$_3$/p-T5H-E-POZ-E	15.7	0.49	53.1	0.51	34.8	28.6	99.2
glass/FAPbI$_3$/p-PET-E-POZ-E	58.5	0.34	18.3	0.66	32.0	31.3	99.3
glass/FAPbI$_3$/PTAA	13.4	0.18	79.9	0.82	67.9	14.5	98.4
glass/FAPbI$_3$/spiro-OMeTAD	10.5	0.49	44.5	0.51	27.8	35.7	99.4

[a] τ_1 and τ_2 represent the time constants of photoluminescence decay, A_1 and A_2 represent the relative amplitudes. The amplitude-weighted average photoluminescence lifetime (τ) was calculated using the equation $\tau = A_1\tau_1 + A_2\tau_2$. The hole extraction rate constant (k_{he}) was determined using the equation $k_{he} = \dfrac{\tau_{PS} - \tau_{HTL}}{\tau_{PS} \times \tau_{HTL}}$. The hole extraction yield (ϕ_{he}) was calculated using the equation $\phi_{he} = \dfrac{\tau_{PS} - \tau_{HTL}}{\tau_{PS}}$, where τ_{PS} represents the amplitude-weighted average photoluminescence lifetime of the glass-supported FAPbI$_3$ film covered with polystyrene (PS), and τ_{HTL} represents the amplitude-weighted average photoluminescence lifetime of the glass-supported FAPbI$_3$ film covered with hole transport layers.
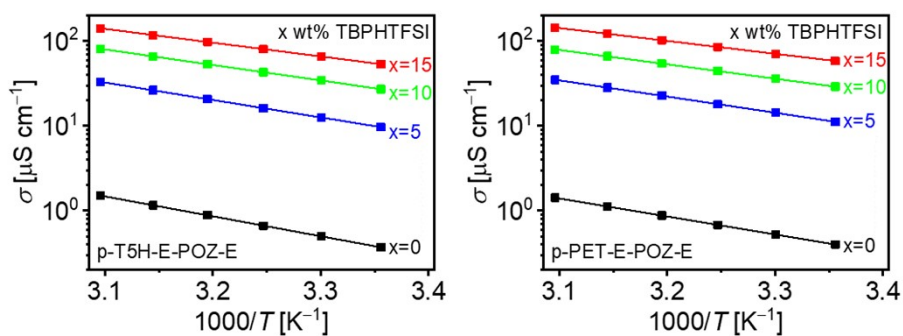
Fig. S7 Arrhenius plots depicting the temperature-dependent electrical conductivity (σ) of semiconducting polymer films containing TBPHTFSI at different weight percentages (x wt%).
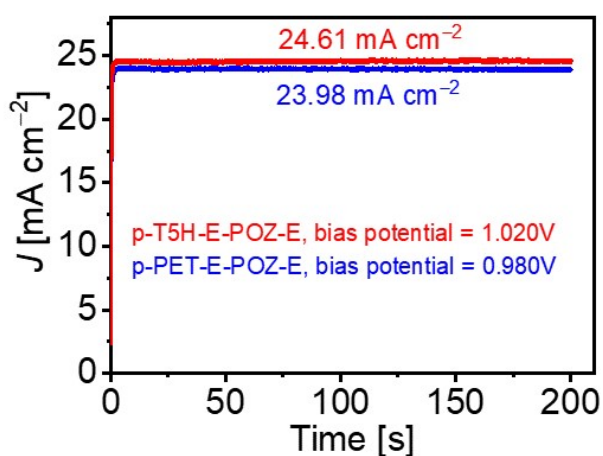
Fig. S8 Steady state outputs of photocurrent density (J).
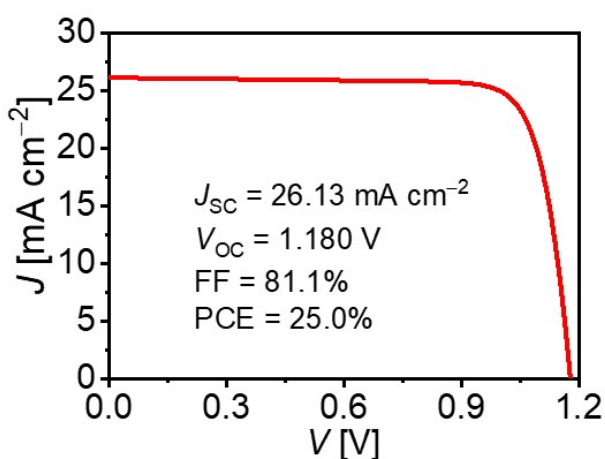
Fig. S9 Representative photocurrent density–voltage (J–V) curve under AM1.5G illumination at 100 mW cm^{-2} for the PSC utilizing fractionated p-T5H-E-POZ-E (M_n = 11.2 kDa, M_w = 17.9 kDa, polymer dispersity index = 1.6).
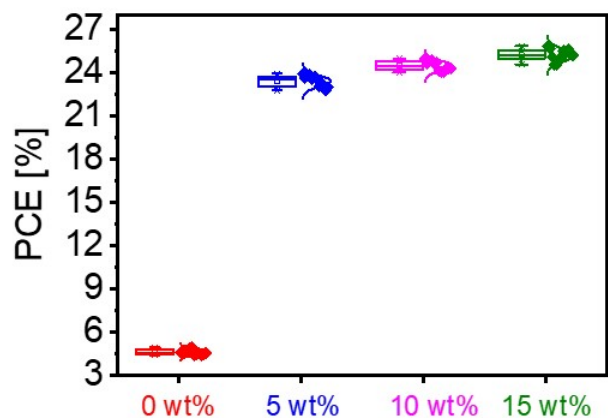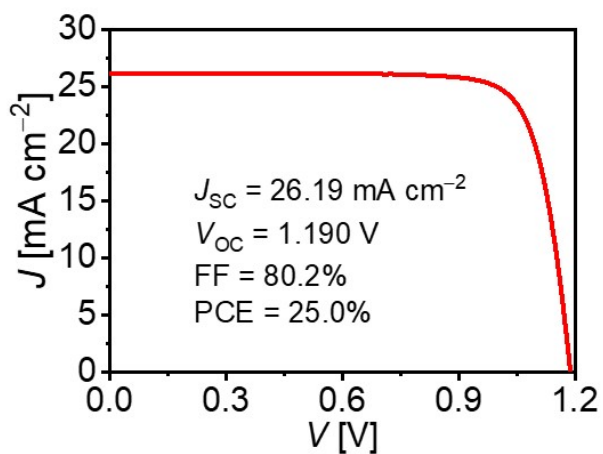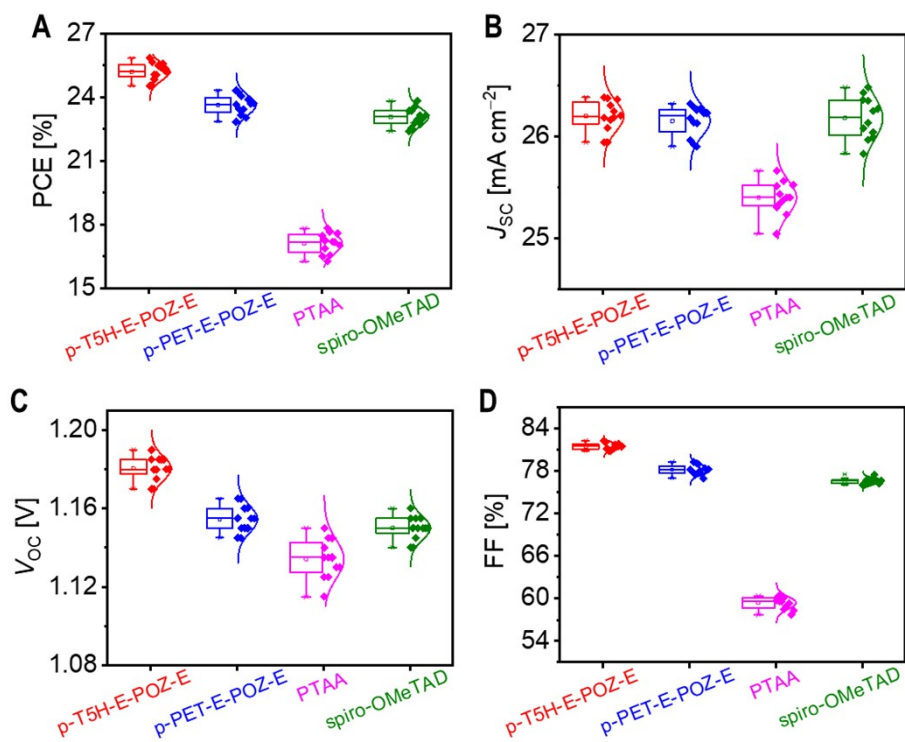
Fig. S10 Power conversion efficiency (PCE) statistics under AM1.5G simulated sunlight irradiation (100 mW cm^{-2}) for the p-T5H-E-POZ-E based cells with varying TBPHTFSI weight percentages.

J_{SC} = 26.19 mA cm^{-2}
V_{OC} = 1.190 V
FF = 80.2%
PCE = 25.0%

Fig. S11 Representative photocurrent density–voltage (J–V) curve under AM1.5G illumination at 100 mW cm^{-2} for the PSC with silver as positive electrode.

Fig. S12 Photovoltaic parameter statistics under AM1.5G simulated sunlight irradiation (100 mW cm^{-2}) for the cells employing different hole transport materials: (A) power conversion efficiency (PCE); (B) short-circuit current density (J_{SC}); (C) open-circuit voltage (V_{OC}); (D) fill factor (FF).
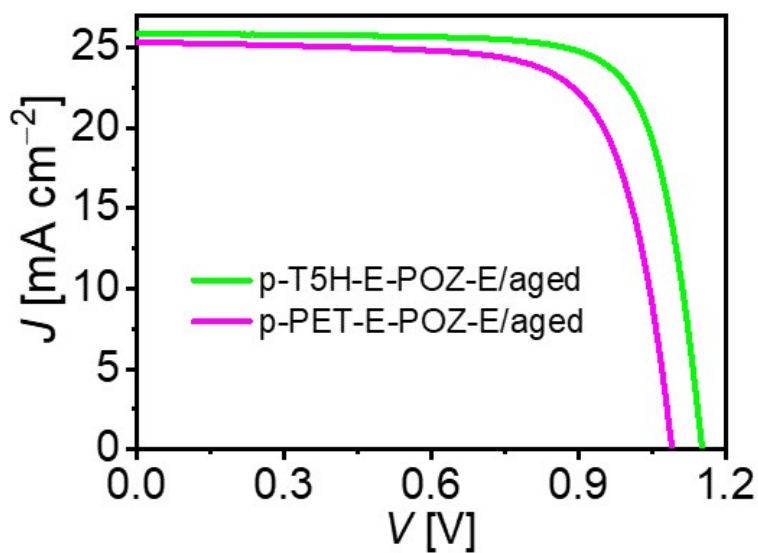
Fig. S13 Representative photocurrent density–voltage (J–V) curves under AM1.5G illumination at 100 mW cm^{-2} for the 1,000-hour, 85°C aged cells.

Table S2. Photovoltaic parameters of representative perovskite solar cells utilizing p-T5H-E-POZ-E and p-PET-E-POZ-E after 1,000-hour, 85°C aging[a]

Cell	J_{SC} [mA cm^{-2}]	V_{OC} [V]	FF [%]	PCE [%]
p-T5H-E-POZ-E/aged	25.91	1.155	76.9	23.0
p-PET-E-POZ-E/aged	25.34	1.090	72.7	20.1

[a] J_{SC}: short-circuit photocurrent density; V_{OC}: open-circuit voltage; FF: fill factor; PCE: power conversion efficiency.

Table S3. Photovoltaic parameters of representative perovskite solar cells based on spiro-OMeTAD and PTAA before and after 1,000-hour 85°C aging[a]

Cell	J_{SC} [mA cm^{-2}]	V_{OC} [V]	FF [%]	PCE [%]
PTAA/unaged	25.43	1.135	59.5	17.2
spiro-OMeTAD/unaged	26.18	1.150	76.7	23.1
PTAA/aged	23.50	1.060	51.6	12.9
spiro-OMeTAD/aged	16.20	0.875	40.9	5.8

[a] J_{SC}: short-circuit photocurrent density; V_{OC}: open-circuit voltage; FF: fill factor; PCE: power conversion efficiency.
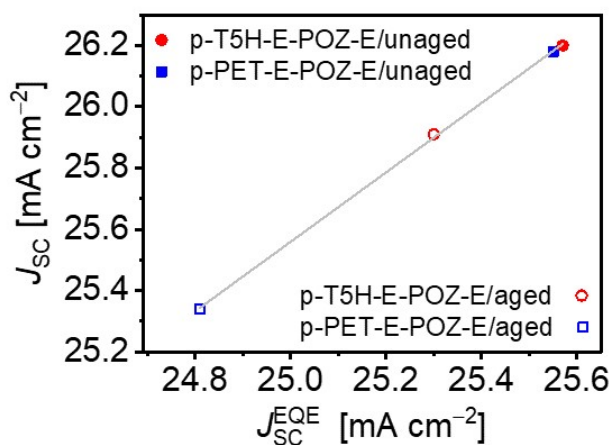
Fig. S14 Correlation between short-circuit photocurrent densities (J_{SC}) obtained from J–V measurements and photocurrent densities derived from EQE spectra (J_{SC}^{EQE}) of both unaged and aged cells. The dataset is fitted with a gray solid line to elucidate the linear relationship.
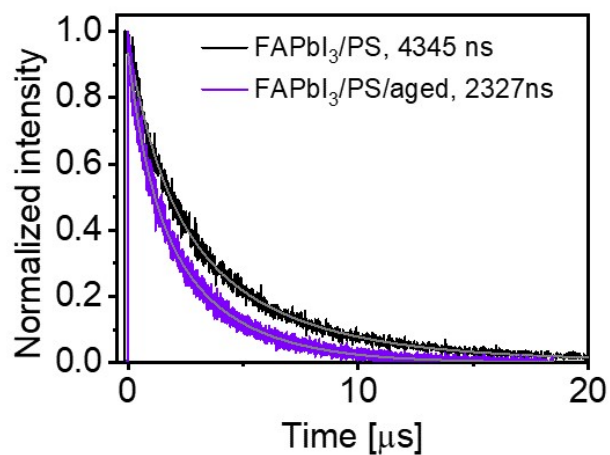
Fig. S15 Time-resolved photoluminescence traces at 810 nm for the dummy cell (glass/FAPbI$_3$/polystyrene/gold) pre- and post-1,000-hour, 85°C aging. Excitation wavelength: 670 nm.
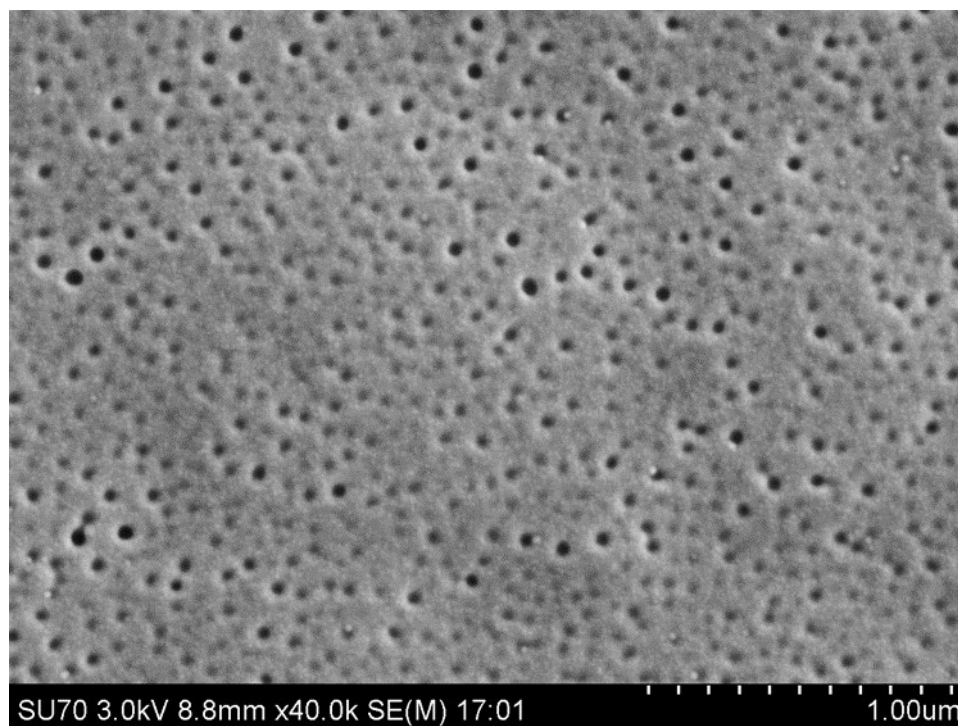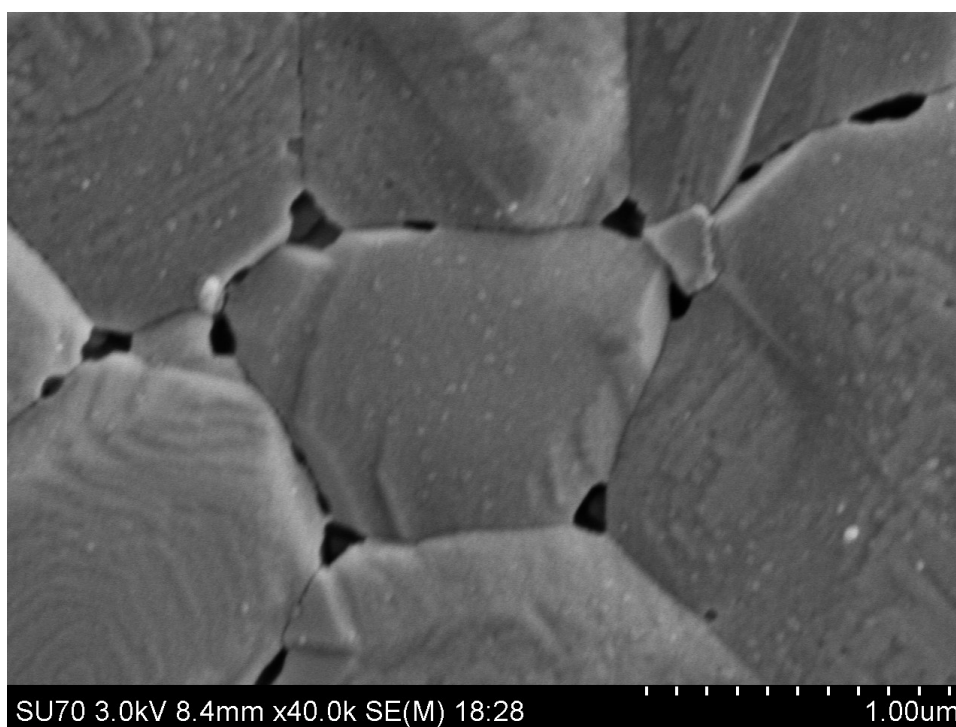

Fig. S16 Top-view scanning electron microscopy image of the hole transport layer in the aged PSC with spiro-OMeTAD. Scale bar: 1 μm. The gold electrode was removed before imaging. Aging was carried out at 85°C for 1,000 h.
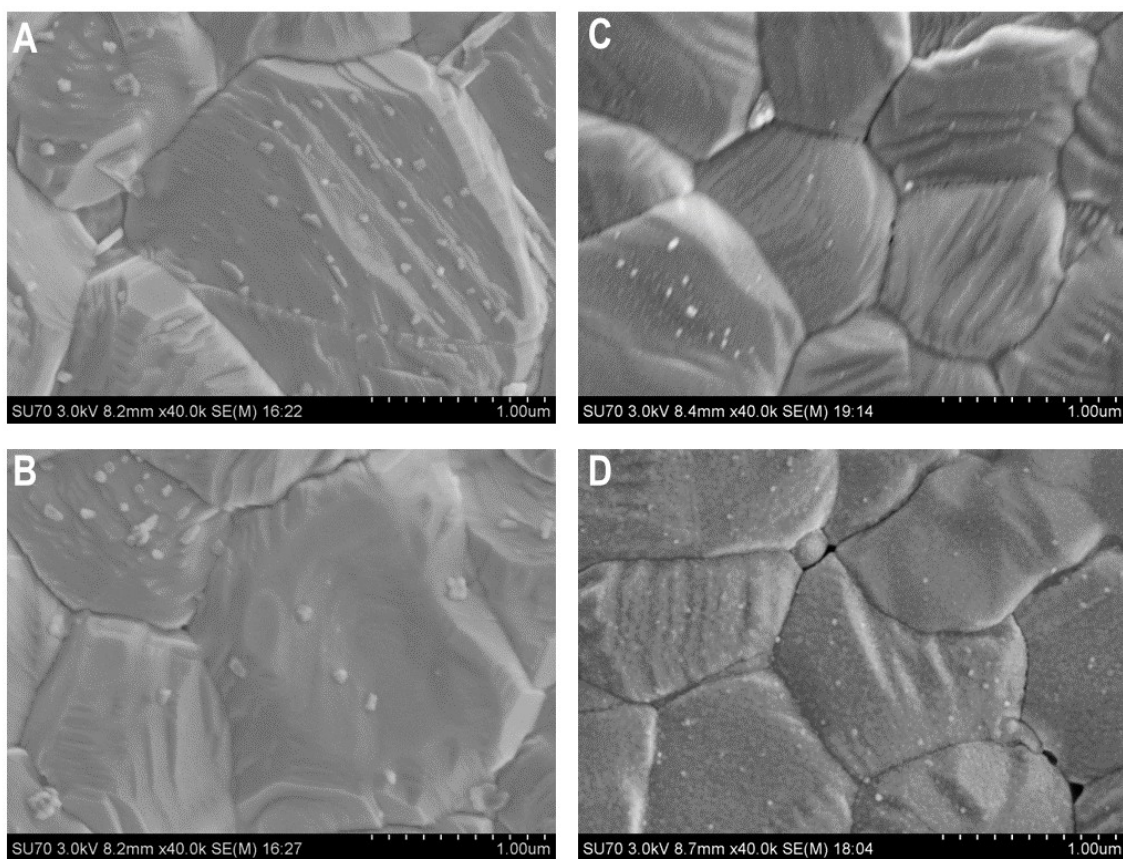
Fig. S17 (A–D) Top-view scanning electron microscopy images of perovskite layers in PSCs pre- and post-aging. (A) the unaged p-T5H-E-POZ-E cell; (B) the unaged p-PET-E-POZ-E cell; (C) the aged p-T5H-E-POZ-E cell; (D) the aged p-PET-E-POZ-E cell. Scale bar: 1 μm. Gold electrodes and HTLs were removed before imaging. Aging was carried out at 85°C for 1,000 h.

Fig. S18 Top-view scanning electron microscopy image of the perovskite layer in the aged PSC with spiro-OMeTAD. Scale bar: 1 μm. The gold electrode and HTL were removed before imaging. Aging was carried out at 85°C for 1,000 h.
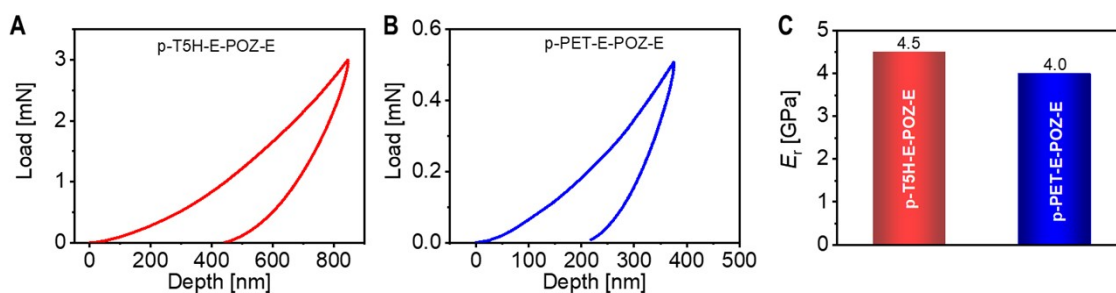
Fig. S19 (A,B) Nanoindentation curves depicting the mechanical behavior of composite thin films incorporating semiconducting polymers and 15 wt% TBPHTFSI. (C) Histogram of Young's modulus (E_r).
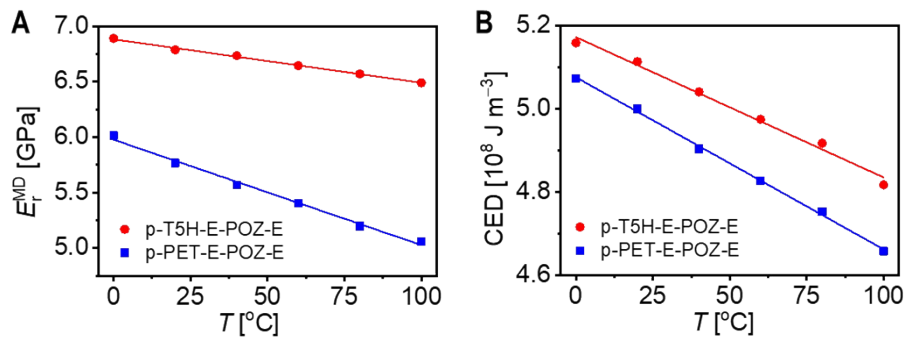
Fig. S20 (A) Plots of molecular dynamics (MD)-simulated Young's modulus (E_r^{MD}) against temperature (T). (B) Plots of MD-simulated cohesive energy density (CED) as a function of T.
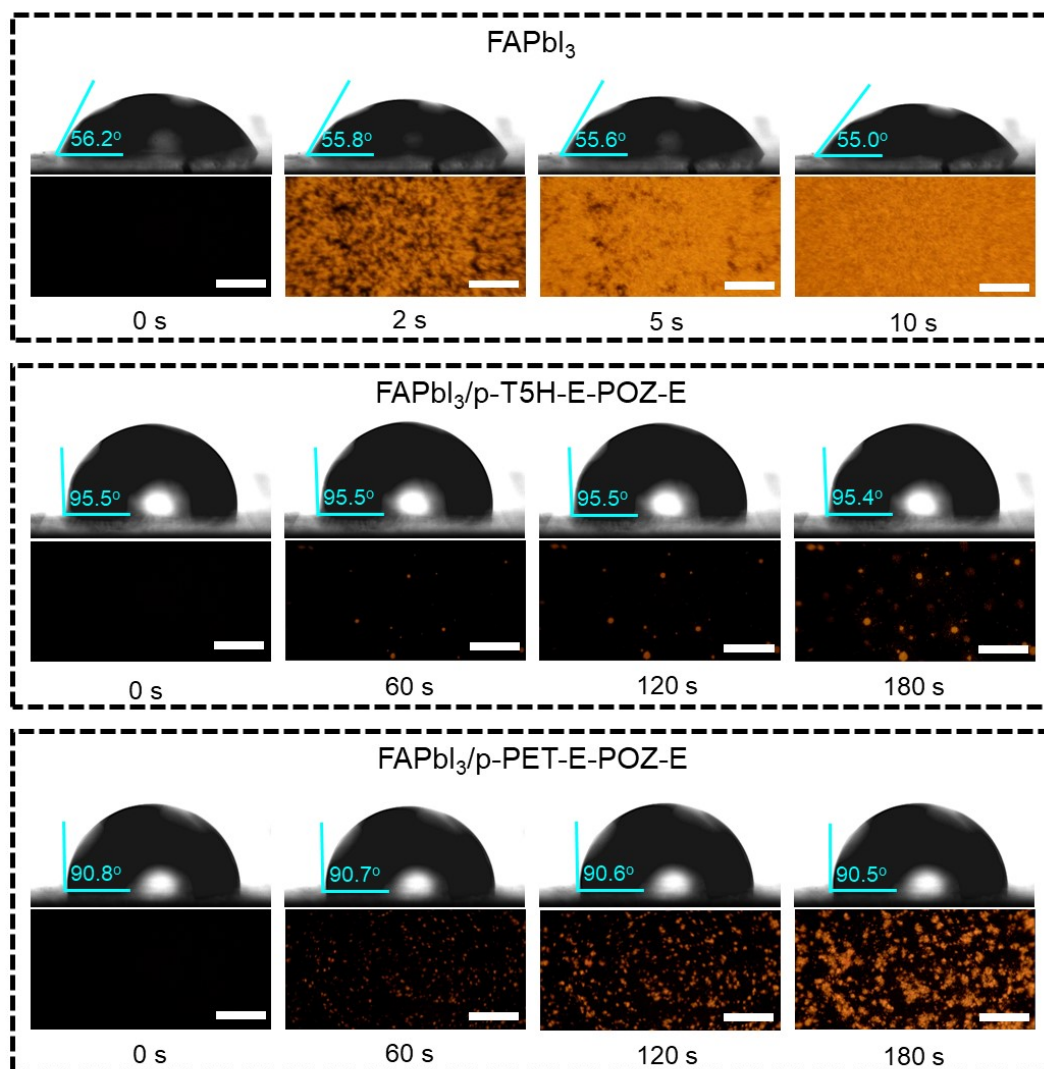
Fig. S21 Temporal evolution of water contact angles and polarizing optical microscope images following the application of a water droplet onto FAPbI$_3$ perovskite film, both uncovered and with polymer coverage. Scale bar: 100 μm.
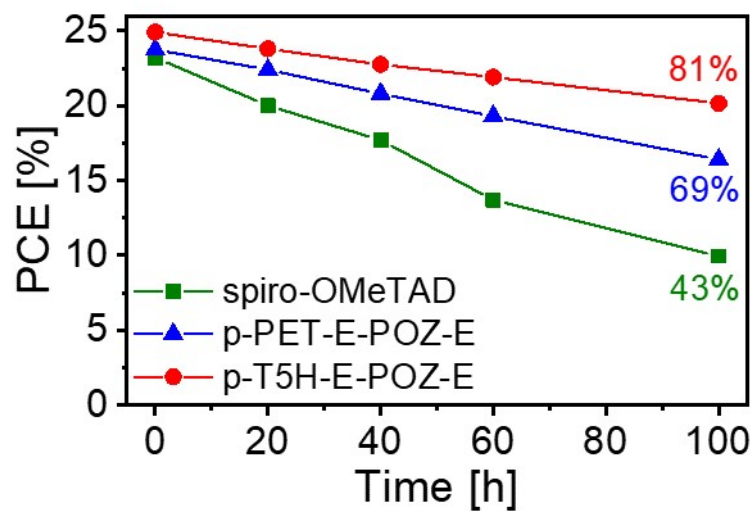
Fig. S22 Evolution of power conversion efficiency (PCE) during exposure to a room temperature environment with humidity levels approaching 100%. Presented are average values from four cells.

4 Appendix: ¹H NMR spectra, ¹³C NMR spectra, ATR-FTIR spectra, UV-vis absorption spectra, and HT-GPC data
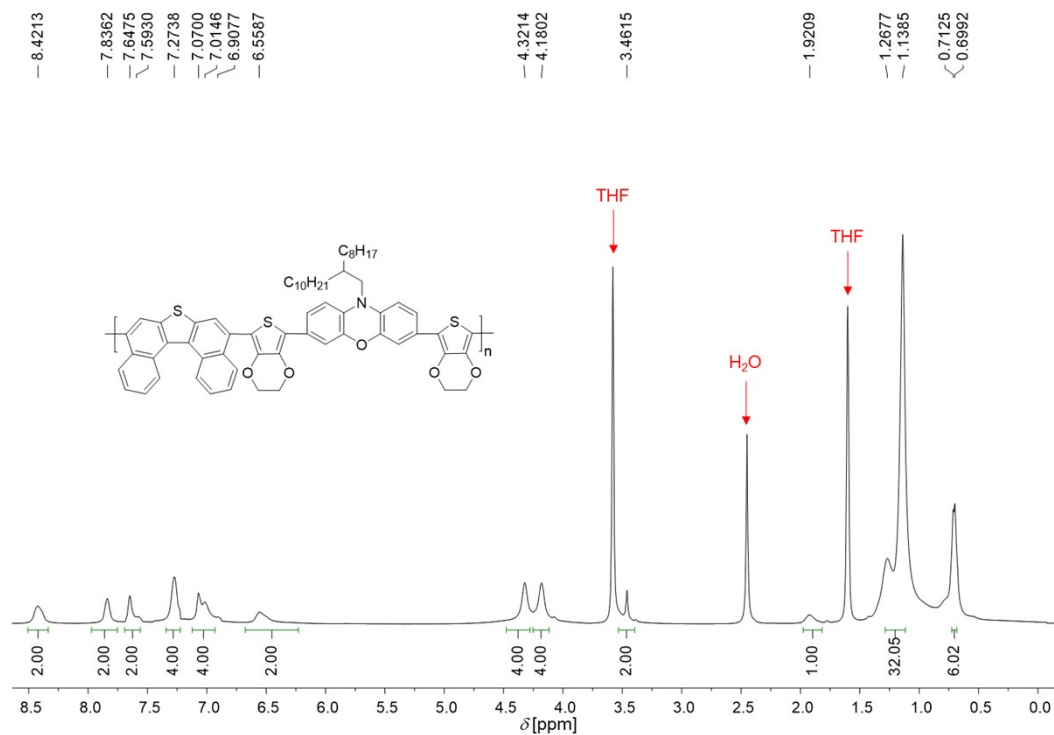
Fig. S23 ¹H NMR (400 MHz) spectrum of p-T5H-E-POZ-E in THF-d_8.
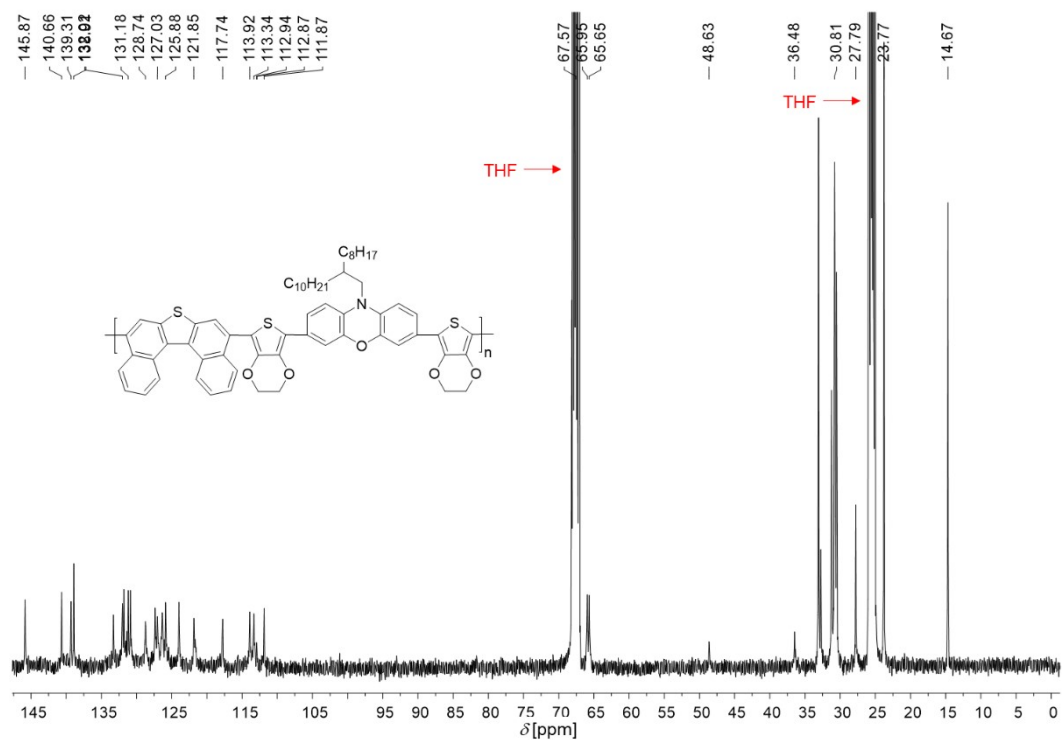
Fig. S24 ¹³C NMR (100 MHz) spectrum of p-T5H-E-POZ-E in THF-d_8.
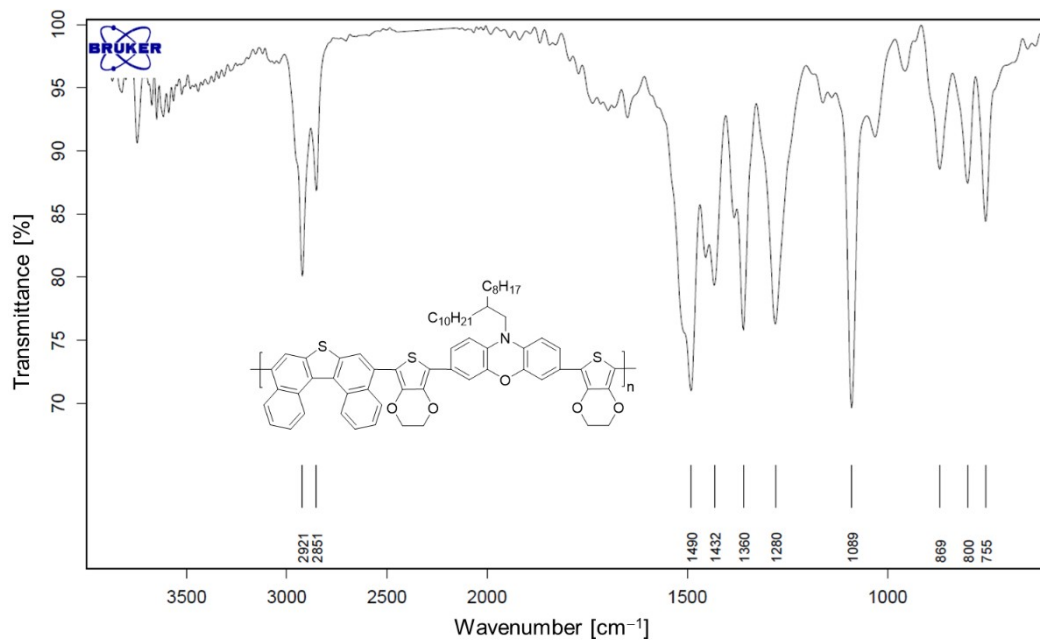
Fig. S25 ATR-FTIR spectrum of p-T5H-E-POZ-E.
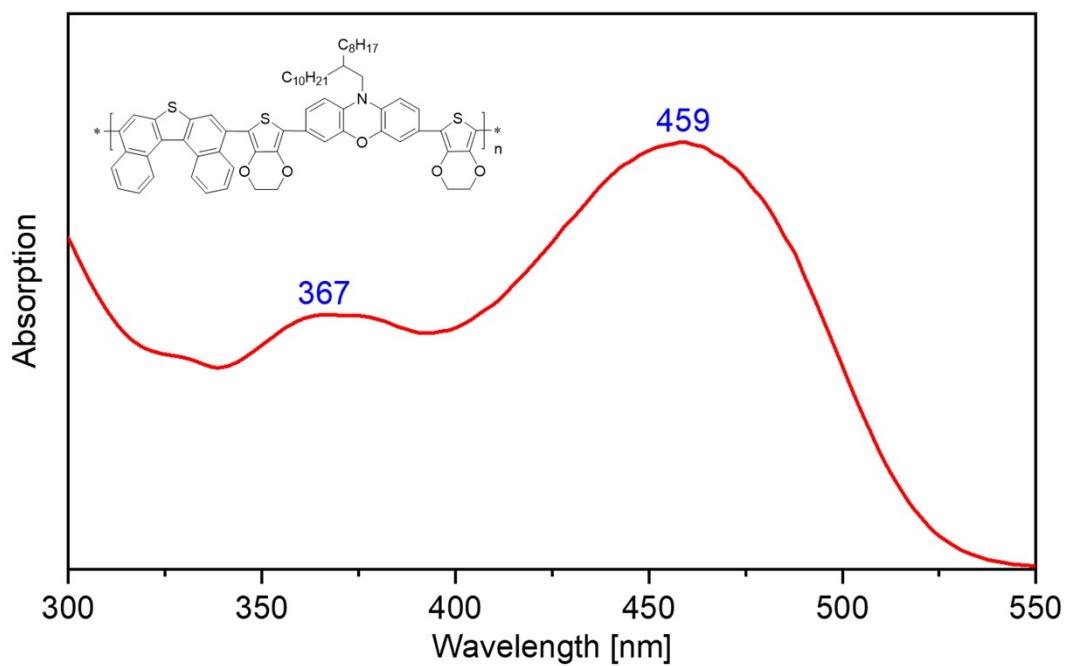
Fig. S26 UV-vis absorption spectrum of p-T5H-E-POZ-E.

Calibration Used: 2023/9/7 9:17:14
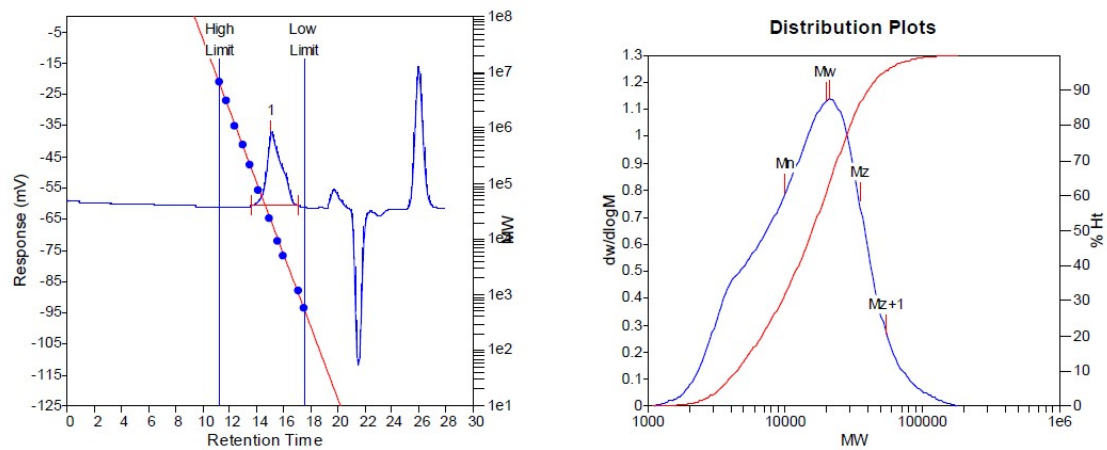
High Limit MW RT: 11.30 mins
High Limit MW: 5833811
K: 17.5000

Low Limit MW RT: 17.52 mins
Low Limit MW: 542
Alpha: 0.6700

MW Averages

Peak No	Mp	Mn	Mw	Mz	Mz+1	Mv	PD
1	21059	9994	19893	34771	54611	17960	1.99049

Fig. S27 HT-GPC data of p-T5H-E-POZ-E.
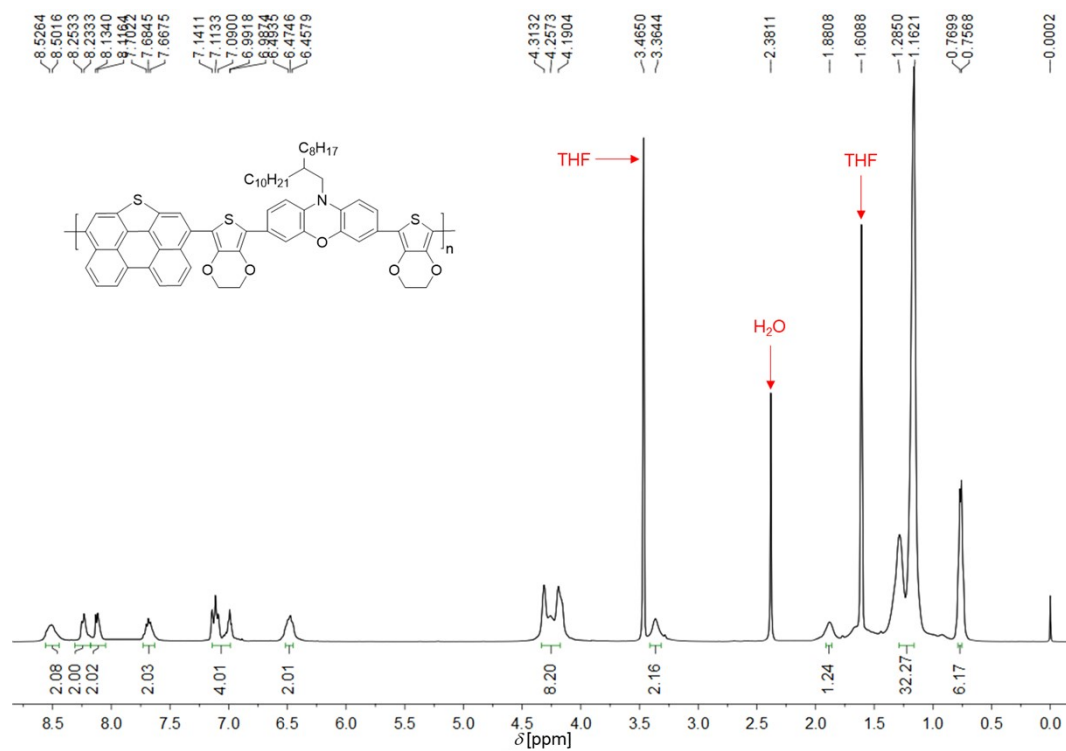
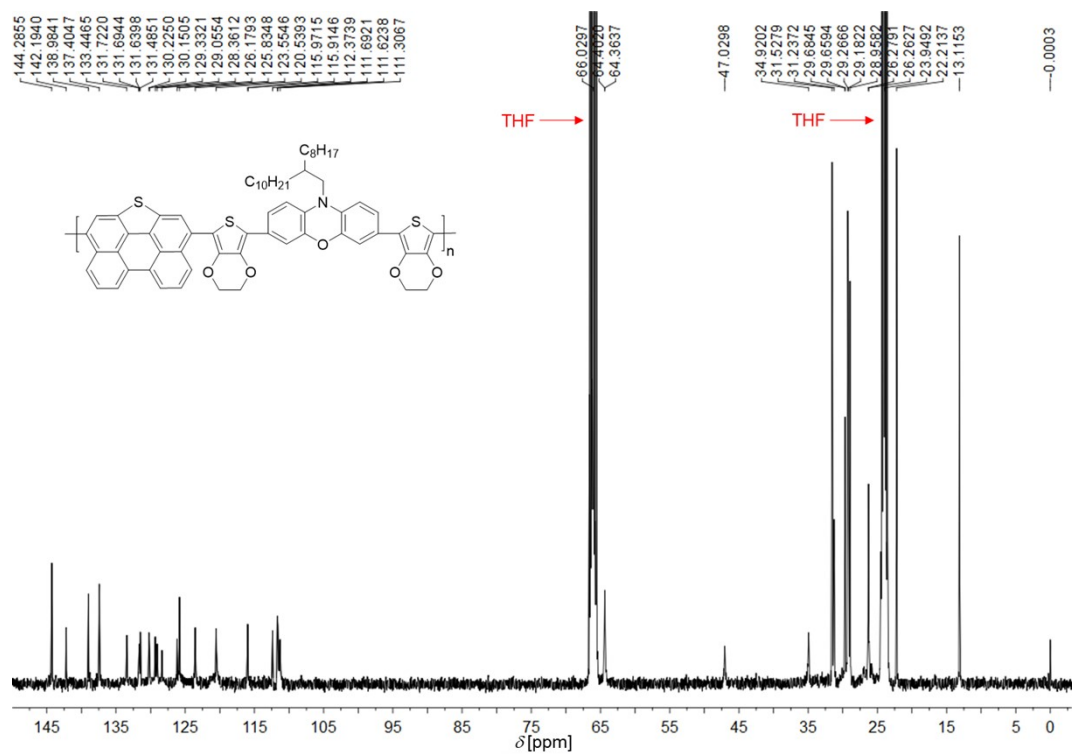**Fig. S28** ^{1}H NMR (400 MHz) spectrum of p-PET-E-POZ-E in THF-d_8.

Fig. S29 ^{13}C NMR (100 MHz) spectrum of p-PET-E-POZ-E in THF-d_8.
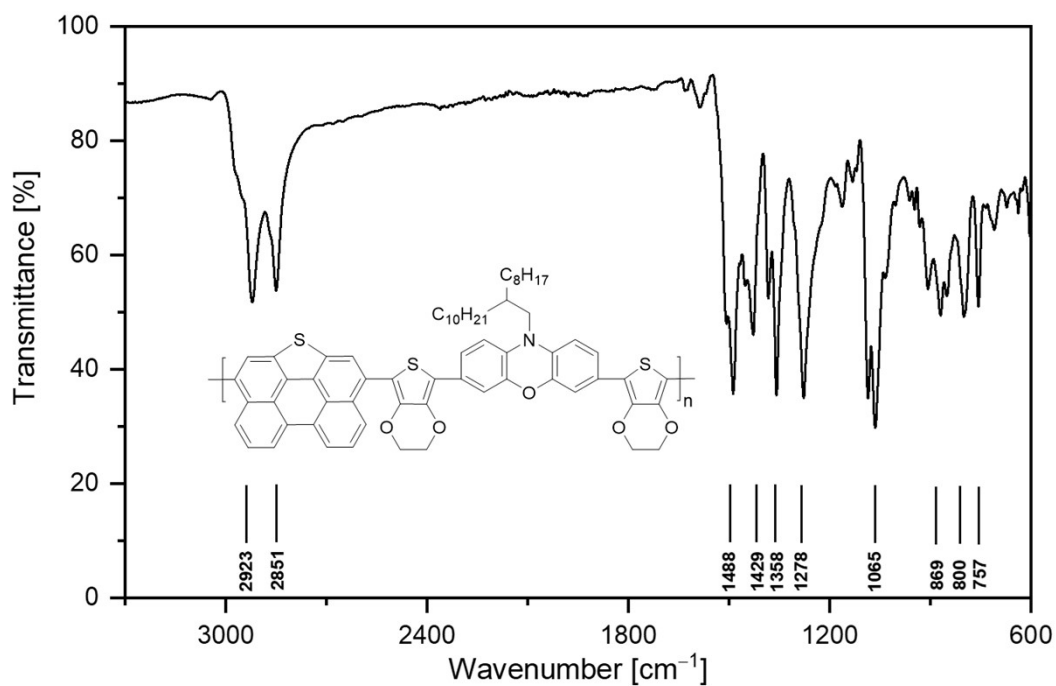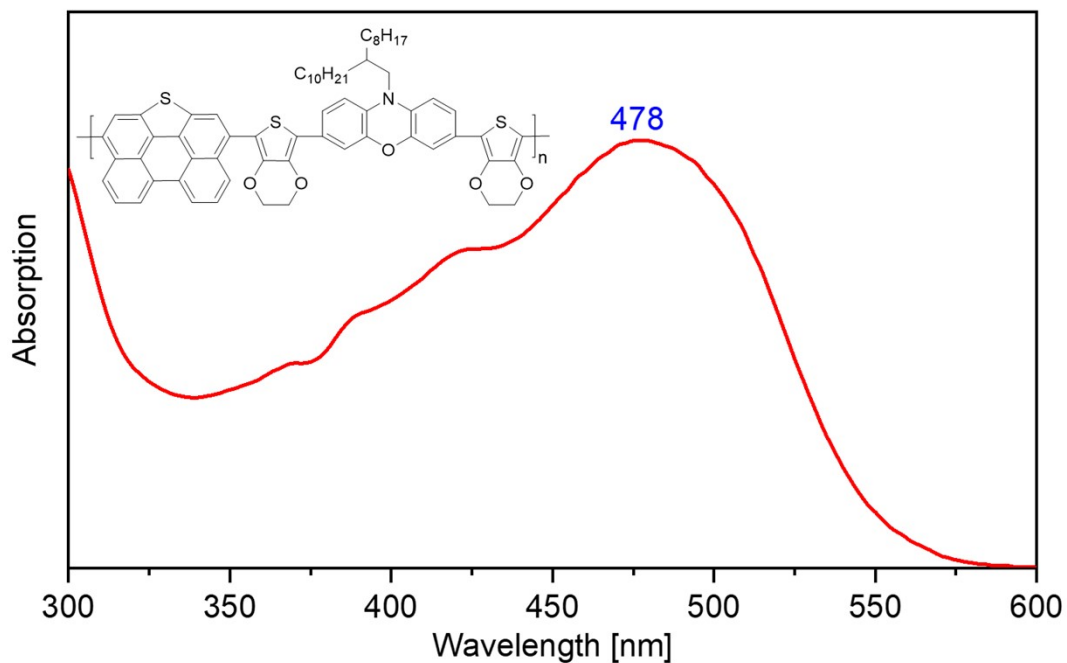

Fig. S30 ATR-FTIR spectrum of p-PET-E-POZ-E.

Fig. S31 UV-vis absorption spectrum of p-PET-E-POZ-E.
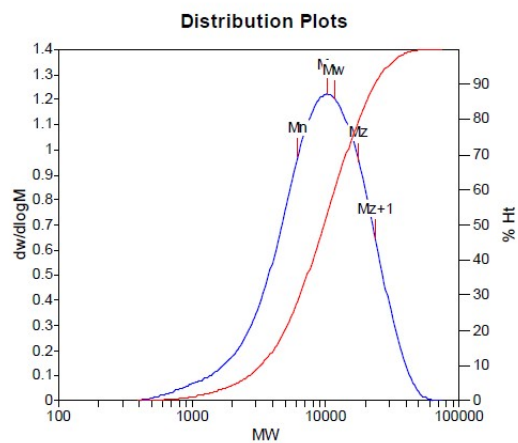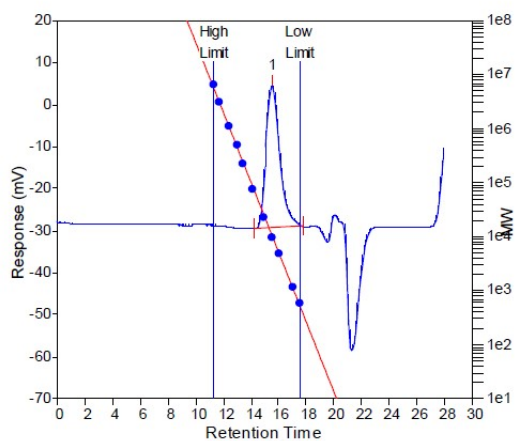
Calibration Used: 2023/9/7 9:17:14

High Limit MW RT: 11.30 mins	Low Limit MW RT: 17.52 mins
High Limit MW: 5833811	Low Limit MW: 542
K: 17.5000	Alpha: 0.6700

MW Averages

Peak No	Mp	Mn	Mw	Mz	Mz+1	Mv	PD
1	10233	6264	11735	17777	23757	10828	1.8734

Fig. S32 HT-GPC data of p-PET-E-POZ-E.

5 References

1 N. Xu, A. Zheng, Y. Wei, Y. Yuan, J. Zhang, M. Lei and P. Wang, *Chem. Sci.*, 2020, **11**, 3418.

2 L. He, Y. Zhang, Y. Wei, Y. Cai, J. Zhang and P. Wang, *Matter*, 2023, **6**, 4013.

3 Y. Ren, M. Ren, X. Xie, J. Wang, Y. Cai, Y. Yuan, J. Zhang and P. Wang, *Nano Energy*, 2021, **81**, 105655.

4 Y. Zhao, F. Ma, Z. Qu, S. Yu, T. Shen, H.-X. Deng, X. Chu, X. Peng, Y. Yuan, X. Zhang and J. You, *Science*, 2022, **377**, 531.

5 Q. Jiang, Y. Zhao, X. Zhang, X. Yang, Y. Chen, Z. Chu, Q. Ye, X. Li, Z. Yin and J. You, *Nat. Photon.*, 2019, **13**, 460.

6 W. C. Oliver and G. M. Pharr, *J. Mater. Res.*, 1992, **7**, 1564.